

Kinematics-Based Detection and Localization of Contacts Along Multisegment Continuum Robots

Andrea Bajo, *Student Member, IEEE*, and Nabil Simaan, *Member, IEEE*

Abstract—In this paper, we present a novel kinematic-based framework for collision detection and estimation of contact location along multisegment continuum robots. Screw theory is used to define a screw motion deviation (SMD) as the distance between the expected and the actual instantaneous screw axis (ISA) of motion. The expected ISA is computed based on the unconstrained kinematics model of the robot, while the actual ISA is computed based on sensory information. Collisions with rigid environments at any point along the robot are detected by monitoring the SMD. Contact locations are estimated by the minimization of the SMD between the ISA that is obtained from a constrained kinematic model of the continuum robot and the one that is obtained from sensor data. The proposed contact detection and localization methods only require the relative motion of each continuum segment with respect to its own base. This strategy allows the straightforward generalization of these algorithms for an n -segment continuum robot. The framework is evaluated via simulations and experimentally on a three-segment multibackbone continuum robot. Results show that the collision-detection algorithm is capable of detecting a single collision at any segment, multiple collisions occurring at multiple segments, and *total-arm* constraint. It is also shown that the estimation of contact location is possible at any location along the continuum robot with an accuracy better than 20% of the segment nominal length. We believe this study will enhance manipulation safety in unstructured environments and confined spaces.

Index Terms—Collision detection, continuum robots, estimation of contact, screw theory.

I. INTRODUCTION

CURRENT robotic systems are incapable of fully characterizing their interaction with the environment. Full characterization of the interaction includes the following: discerning collisions, localizing contact constraints, and estimating interaction forces. Although there are mature algorithms for compliant hybrid motion/force control [1]–[5], there exists no unified framework for the *impact* and *postimpact* phases. These algorithms require *a priori* knowledge of the environmental con-

straint geometry via the formulation of natural and artificial constraints [6] or motion and constraint screws [7]–[9].

Previous works individually focused on collision detection [10], [11] and estimation of constraint locations [12]–[14]. In [10] and [11], the generalized momentum of serial robots was used to identify contact incidence and the link at which contact occurs. In [12], a least-squares method using the estimate of contact location from tactile sensors and joint torque measurements to estimate the magnitude and the location of contact force was proposed. In [13] and [14], two different probabilistic approaches for contact estimation were presented. Other researchers tried to overcome the limitations of rigid-link robots by developing sensitive robotic skins [15].

Continuum robots are *continuously bending, infinite-degree-of-freedom elastic structures* [16] that offer an opportunity to overcome the limitations of rigid-link robots. This opportunity stems from the ability of continuum robots to change their natural shape, when interacting with the environment. The goal of this paper is to capture this information and provide a general framework for collision detection and contact-location estimation along multisegment continuum robots.

The motivation behind this study originates in the field of medical robotics. The onus of safeguarding against surgical trauma currently lies on the surgeon. New surgical paradigms, such as natural orifice transluminal endoscopic surgery (NOTES), demand deeper anatomical reach along increasingly tortuous paths and often require multiple tools to safely coexist in confined surgical site. This added complexity requires *intelligent* surgical slaves that are able to detect collisions with other surgical effectors and the surrounding anatomy to prevent inadvertent trauma to the patient and to the end effectors. These robots will need to support automated or semiautomated insertion into the anatomy, estimate contact locations along their structure, regulate their contact forces, and use their multipoint interactions to enhance end-effector precision and safety. With this goal in mind, researchers have relied on passive compliance of continuum robots [17]–[20] and wire-actuated robots [21]. However, reliance on passive compliance of surgical robots comes with a price of performance degradation in terms of payload carrying capability and position accuracy.

This paper complements previous works that provide continuum robots with the ability to act as sensors, as well as surgical intervention platforms. In [22], the authors proposed and validated a method for the estimation of wrenches at the tip of multisegment continuum robots, such as the one that is shown in Fig. 1. In [23], the problem of contact detectability using joint-level force measurements and the fixed centrodices of instantaneous planar motion for a single-segment continuum robot was

Manuscript received April 18, 2011; revised October 23, 2011; accepted October 31, 2011. Date of publication December 8, 2011; date of current version April 9, 2012. This paper was recommended for publication by Associate Editor Y. Choi and Editor B. J. Nelson upon evaluation of the reviewers' comments. The work was supported by the National Science Foundation under Career Grant IIS-1063750.

The authors are with the Department of Mechanical Engineering, Vanderbilt University, Nashville, TN 37212 USA (e-mail: andrea.bajo@vanderbilt.edu; nabil.simaan@vanderbilt.edu).

This paper has supplementary downloadable material available at <http://ieeexplore.ieee.org>.

Color versions of one or more of the figures in this paper are available online at <http://ieeexplore.ieee.org>.

Digital Object Identifier 10.1109/TRO.2011.2175761

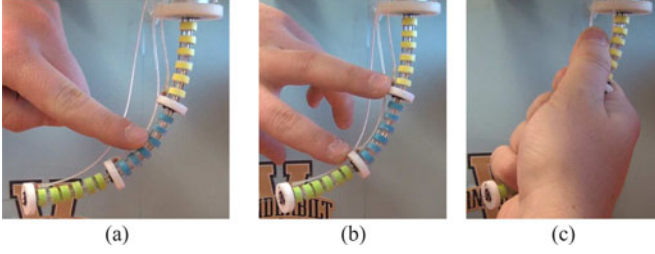


Fig. 1. Multisegment continuum robot detecting (a) single collision, (b) multiple collisions, and (c) total-arm constraint.

investigated. In [24], an approach for compliant motion control that does not require explicit estimation of interaction forces and *a priori* knowledge of their location was presented. To the best of the authors' knowledge, no algorithms exist for detection and localization of contacts along multisegment continuum robots.

The contribution of this paper is to present a general framework for collision detection and contact estimation for an *n*-segment continuum robot. The framework relies only on the relative motion of each segment with respect to its own base. By working in local frames, collision detection and estimation of contact location are generalized for multisegment continuum robots. A *screw motion Deviation* (SMD) is proposed based on the nominal forward kinematics of the robot and extrinsic sensory information. Online calculation of this deviation for each segment enables single-collision and multicollision detection at multiple segments. The estimation of contact location is carried out by using a constrained kinematics model that describes the constrained motion of the continuum robot. Results demonstrate the ability of estimating the location of contacts, detecting collisions at any point along the robotic structure [see Fig. 1(a)], multiple collisions acting at different segments [see Fig. 1(a)], and *total arm* constraint [see Fig. 1(c)].

II. PROBLEM STATEMENT AND ASSUMPTIONS

This study is relevant for multisegment continuum robots that bend in a known, repeatable shape. Example of such robots are active catheters [20], tentacle/trunk robots [25], and multibackbone continuum robots as in Fig. 1. These robots are composed of multiple independently actuated flexible segments. Each continuum segment (CS) is composed of a base disk (BD), several spacer disks (SD), an end disk (ED), and wires or backbones depending on the particular actuation system. In the case of multibackbone continuum robots, the primary backbone is centrally located in each SD. *m* secondary backbones are evenly distributed around the central backbone with the division angle: $\beta = 2\pi/m$. The secondary backbones are only attached to the ED, and they are used to bend the CS using the push-pull actuation. An example of a multisegment continuum robot, where each segment bends in a circular shape, is shown in Fig. 1.

A. Problems

P1—Collision Detection: Given a multisegment continuum robot, find a general strategy for contact detection that includes a characterization of the constrained movement of the robot.

P2—Estimation of Contact Location: Once the collision is detected, identify the segment at which the constraint occurs and estimate the location of contact along the CS.

B. Assumptions

A1: Each CS bends in a circular shape and the gravitational forces are negligible. These assumptions were verified, respectively, in [26] and [27], for small continuum robots.

A2: The pose of each segment's ED is available. Such information may be obtained using a vision system as in [28] and [29] or a magnetic tracker device as in [30].

A3: A distally constrained segment will affect the motion of all proceeding segments, while a proximal constrained segment will not affect the motion of subsequent distal segment. This assumption is experimentally verified in this study.

A4: After collision with a stationary obstacle, the constrained portion of a segment (see Fig. 2) maintains a fixed circular shape, and the remainder of the segment continues to bend in the same fashion as a shorter segment.

III. CONSTRAINED KINEMATICS

In this section, we introduce the constrained kinematics of a CS in point contact at an arbitrary arc-length location, i.e., $\sigma_k \in [0, L_k]$, along the primary backbone immediately after the constraint is applied under assumptions A1, A3, and A4. The forward kinematics of the unconstrained CS was presented in [31]. The kinematics nomenclature is illustrated in Fig. 2 and defined in detail in Table I.

A. Constrained Direct Kinematics

Immediately after the *k*th CS collides ($k = 1, \dots, n$), the position $\mathbf{p}_{c_k}^{b_k}$ and orientation $\mathbf{R}_{c_k}^{b_k}$ of the contact frame $\{C_k\}$ (see Fig. 2) with respect to a local base frame $\{B_k\}$ is given by

$$\mathbf{p}_{c_k}^{b_k} = \mathbf{R}_{p_k}^{b_k} \frac{L_k}{\theta_0 - \theta_{L_k}(t_c)} \begin{bmatrix} 1 - \sin \theta_{\sigma_k} \\ 0 \\ \cos \theta_{\sigma_k} \end{bmatrix} \quad (1)$$

$$\mathbf{R}_{c_k}^{b_k} = \mathbf{R}_{p_k}^{b_k} \mathbf{R}_{e_k}^{p_k} \mathbf{R}_{c_k}^{e_k} \quad (2)$$

where $\mathbf{R}_{p_k}^{b_k} = e^{-\delta_k(t_c)\mathbf{e}_3 \times}$, $\mathbf{R}_{e_k}^{p_k} = e^{(\theta_0 - \theta_{\sigma_k})\mathbf{e}_2 \times}$, and $\mathbf{R}_{c_k}^{e_k} = e^{\delta_k(t_c)\mathbf{e}_3 \times}$ denote the exponential forms for these rotations; \mathbf{e}_2 and \mathbf{e}_3 are the canonical unit vectors along the *y*- and *z*-axes; $\theta_{L_k}(t_c)$ is the bending angle at the time of contact t_c , and θ_{σ_k} is given by

$$\theta_{\sigma_k} = \theta_0 - \frac{\sigma_k}{L_k} (\theta_0 - \theta_{L_k}(t_c)) \quad (3)$$

Using (1), (2), and assumption A4, the position $\mathbf{p}_{g_k}^{b_k}$ and orientation $\mathbf{R}_{g_k}^{b_k}$ of the ED of the constrained segment is given by

$$\mathbf{p}_{g_k}^{b_k} = \mathbf{p}_{c_k}^{b_k} + \mathbf{R}_{c_k}^{b_k} \mathbf{R}_{f_k}^{c_k} \frac{L_k - \sigma_k}{\Theta_k} \begin{bmatrix} 1 - \cos \Theta_k \\ 0 \\ \sin \Theta_k \end{bmatrix} \quad (4)$$

$$\mathbf{R}_{g_k}^{b_k} = \mathbf{R}_{c_k}^{b_k} \mathbf{R}_{f_k}^{c_k} \mathbf{R}_{h_k}^{f_k} \mathbf{R}_{g_k}^{h_k} \quad (5)$$

TABLE I
KINEMATICS NOMENCLATURE

symbol	description
m	Number of secondary backbones in each segment
i	Index of the secondary backbones, $i=1,2,m$
n	Number of continuum segments
k	Index of the robot's segments, $k=1,\dots,n$
s_k	Arc-length parameter of the primary backbone of segment k
L_k	Nominal length of the primary backbone of segment k
σ_k	Arc-length specifying the contact location along the primary backbone, $\sigma_k \in [0, L_k]$
r	The radius of the pitch circle on which the secondary backbones are equally distributed with division angle β around the primary backbone
β	The division angle by which the secondary backbones are equally distributed around the primary backbone. $\beta = 2\pi/m$
$\theta_k(s_k)$	The angle of the tangent to the primary backbone in the bending plane. $\theta_k(s_k = L_k)$, $\theta_k(s_k = \sigma_k)$, and $\theta_k(s_k = 0)$ are designated by θ_{L_k} , θ_{σ_k} , and $\theta_0 = \pi/2$ respectively. Note that θ_{L_k} is the commanded bending angle of the unconstrained segment
δ_k	The commanded right-handed rotation angle from \mathbf{x}_{p_k} about \mathbf{z}_{b_k} to a line pointing from the center of the base and passing through the primary backbone of the i^{th} secondary backbone of segment k at $s_k = 0$
t_c	Instant of contact. NOTE: $\delta_k(t_c)$ and $\theta_{L_k}(t_c)$ denotes the commanded angles δ_k and θ_{L_k} at time t_c
ψ_k	Commanded configuration space vector of unconstrained segment k . $\psi_k \triangleq [\theta_{L_k} \quad \delta_k]^T$
ψ	Augmented configuration space vector for an n -segment continuum robot $\psi \triangleq [\psi_1^T \quad \dots \quad \psi_n^T]^T$
\mathbf{q}_k	Joint-space vector of CS k . $\mathbf{q}_k \triangleq [q_1 \quad \dots \quad q_m]^T$
\mathbf{q}	Augmented joint-space vector of the continuum robot. $\mathbf{q} \triangleq [q_1 \quad \dots \quad q_n]^T$
$[\mathbf{u} \times]$	Skew-symmetric matrix of vector $\mathbf{u} = [u_x \quad u_y \quad u_z]^T$. $[\mathbf{u} \times] \triangleq \begin{bmatrix} 0 & -u_z & u_y \\ u_z & 0 & -u_x \\ -u_y & u_x & 0 \end{bmatrix}$
$\{B_k\}$	Segment's base frame. The x-axis \mathbf{x}_{b_k} points from the center of the base disk to the first secondary backbone
$\{P_k\}$	This frame is obtained from $\{B_k\}$ by a rotation of $-\delta_k(t_c)$ about \mathbf{z}_{b_k}
$\{E_k\}$	This frame is obtained from $\{P_k\}$ by a translation of $\mathbf{p}_{c_k}^{b_k}$ and a rotation of $\theta_0 - \theta_{\sigma_k}$ about \mathbf{y}_{p_k}
$\{C_k\}$	Contact frame. This frame is obtained from $\{E_k\}$ by a rotation of δ_k about \mathbf{z}_{e_k}
$\{F_k\}$	This frame is obtained from $\{C_k\}$ by a rotation about $-\delta_k(t)$ about \mathbf{z}_{c_k}
$\{H_k\}$	This frame is obtained from $\{F_k\}$ by a translation of $\mathbf{p}_{g_k}^{b_k} - \mathbf{p}_{c_k}^{b_k}$ (Fig. 2) and a rotation of $\Theta_k \triangleq \theta_{\sigma_k} - \theta_{L_k}$ about \mathbf{y}_{h_k}
$\{G_k\}$	Gripper frame. This frame is obtained from $\{H_k\}$ by a rotation of δ_k about \mathbf{z}_{h_k}
$\mathbf{v}_{g_k/b_k}^{b_k}$	Translational velocity of $\{G_k\}$ with respect to $\{B_k\}$ in $\{B_k\}$
$\omega_{g_k/b_k}^{b_k}$	Angular velocity of $\{G_k\}$ with respect to $\{B_k\}$ in $\{B_k\}$
$\mathbf{J}_{v\psi_k}$	Constrained translational Jacobian that relates $\dot{\psi}_k$ to $\mathbf{v}_{g_k/b_k}^{b_k}$
$\mathbf{J}_{\omega\psi_k}$	Constrained angular Jacobian that relates $\dot{\psi}_k$ to $\omega_{g_k/b_k}^{b_k}$
$\mathbf{J}_{q\psi_k}$	Jacobian matrix that relates $\dot{\psi}_k$ to $\dot{\mathbf{q}}_k$
$\mathbf{J}_{q\psi}$	Jacobian matrix that relates $\dot{\psi}$ to $\dot{\mathbf{q}}$

By taking the time derivatives of both sides of (13), the instantaneous inverse kinematics of segment k is given by

$$\dot{\mathbf{q}}_k = \mathbf{J}_{q\psi_k} \dot{\psi}_k. \quad (14)$$

Hence, for an n -segment continuum robot, the joint-space kinematics is given by

$$\dot{\mathbf{q}} = \mathbf{J}_{q\psi} \dot{\psi} \quad (15)$$

where

$$\mathbf{J}_{q\psi} = \mathbf{G} \begin{bmatrix} \mathbf{J}_{q\psi_1} & \mathbf{0} & \dots & \mathbf{0} \\ \mathbf{0} & \mathbf{J}_{q\psi_2} & \ddots & \vdots \\ \vdots & \ddots & \mathbf{J}_{q\psi_k} & \mathbf{0} \\ \mathbf{0} & \dots & \mathbf{0} & \mathbf{J}_{q\psi_n} \end{bmatrix} \quad (16)$$

and $\dot{\psi} \triangleq [\dot{\psi}_1^T \quad \dots \quad \dot{\psi}_n^T]^T \in \mathbb{R}^{2n \times 1}$ is the time derivative of the augmented configuration space vector for a robot with n independent segments, and $\dot{\mathbf{q}} \triangleq [\dot{\mathbf{q}}_1^T \quad \dots \quad \dot{\mathbf{q}}_n^T]^T \in \mathbb{R}^{nm \times 1}$ is the augmented vector of the instantaneous joint velocities. The matrix $\mathbf{G} \in \mathbb{R}^{nm \times nm}$ accounts for actuation coupling among subsequent segments. For example, if the actuator of the m th backbone in the segment $k+1$ is serially attached to the actuator of the m th backbone in the segment k , then $\mathbf{G} = \mathbf{I}$. In this case, the actuation unit design is decoupled.

IV. SCREW MOTION DEVIATION

This section defines a motion deviation using screw theory. In the following, the mathematical entities that constitute the instantaneous screw of motion of a rigid body are summarized from [33]–[35]. As a consequence of Chasles's theorem [35], the instantaneous motion of a rigid body is fully described by the *Plücker line coordinates* [35] of the instantaneous screw axis (ISA) and the screw pitch. Thus, the following three entities describe the motion of ED k with respect to local base frame $\{B_k\}$:

$$\mathbf{r}_k = \frac{\omega_{g_k/b_k}^{b_k} \times (\mathbf{v}_{g_k/b_k}^{b_k} + p_{g_k}^{b_k} \times \omega_{g_k/b_k}^{b_k})}{\|\omega_{g_k/b_k}^{b_k}\|^2} \quad (17)$$

$$\hat{\omega}_k = \frac{\omega_{g_k/b_k}^{b_k}}{\|\omega_{g_k/b_k}^{b_k}\|} \quad (18)$$

$$\lambda_k = \frac{\hat{\omega}_k^T (\mathbf{v}_{g_k/b_k}^{b_k} + p_{g_k}^{b_k} \times \omega_{g_k/b_k}^{b_k})}{\|\omega_{g_k/b_k}^{b_k}\|} \quad (19)$$

where vector \mathbf{r}_k locates the closest point on the screw axis relative to the origin, $\hat{\omega}_k$ is the unit vector along the axis, and λ_k is the screw pitch.

Note that, in general case of rigid body motion, (17), (18), and (19) are ill-defined, when $\|\omega_{g_k/b_k}^{b_k}\| = 0$. The screw axis lies along the direction of translational velocity, and $\lambda_k = 0$. However, because of the constrained bending shape of the CS, $\mathbf{v}_{g_k/b_k}^{b_k}$ and $\omega_{g_k/b_k}^{b_k}$ always vanish simultaneously. This means that during motion, $\|\omega_{g_k/b_k}^{b_k}\|$ is never equal to zero, and the special case can be excluded.

A better way to compute vector \mathbf{r}_k is given by the following least-squares approximation [34]:

$$\mathbf{r}_k = \mathbf{A}^\dagger \mathbf{b} \quad (20)$$

where superscript “ \dagger ” indicates the left pseudoinverse, and

$$\mathbf{A} = [\Omega_{g_k/b_k}^T \quad \omega_{g_k/b_k}^{b_k T}]^T \quad (21)$$

$$\mathbf{b} = [\Omega_{g_k/b_k} \mathbf{p}_{g_k}^{b_k} - \Lambda \mathbf{v}_{g_k}^{b_k} \quad 0]^T \quad (22)$$

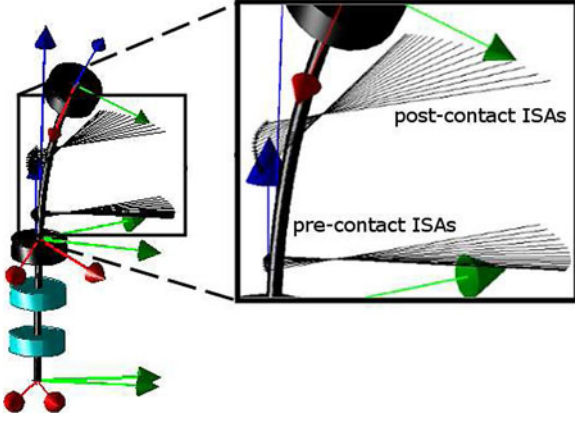


Fig. 3. Group of ISAs after the contact is appreciably shifted toward the ED of the segment because of the smaller radius of curvature of the unconstrained portion of the segment. The closer the disk in contact is to the end disk, the closer the postcontact ISAs will be to the end disk.

$\Lambda = \mathbf{I} - \omega_{g_k/b_k}^{b_k} \omega_{g_k/b_k}^{b_k T} / \|\omega_{g_k/b_k}^{b_k}\|^2$, and \mathbf{I} is the 3×3 identity matrix.

Using (18) and (20), one obtains the *axode* of motion [36] that is associated with the motion of the k th ED. As a consequence of a collision, the axode of motion suddenly shifts as shown in Fig. 3. The figure shows the abrupt gap between *precontact* ISAs and *postcontact* ISAs when applying the constraint at the third SD. A 3-D computer simulation of the shift of the axode of motion is also shown in multimedia extension I, which shows a scenario, where a CS contacts the environment at its third SD. The constrained portion of the segment remains fixed, while the unconstrained portion bends as a shorter segment with nominal length $L_k - \sigma_k$.

Various approaches can be used to quantify the difference between two infinitesimally separated screws. Since the screw axis is essentially a line, one possible way is to use a Riemannian metric as described in [37]. For spatial motion, the natural generalization of the curve of centres used in [23] is given by what is called the *striction curve* [38]. An approximation of the striction curve is obtained by the concatenation of the closest points between infinitesimally separated screw axes. These pairs of points are obtained by the intersection of two consecutive screw axes and their common normal. The striction curve was used in [39] to classify knee pathologies. However, the striction curve is ill-defined when the CS bends in a fixed plane. In fact, during planar motion, the ISAs are all perpendicular to the bending plane, and there are infinite pairs of points that define the minimum distance between the axes. In this case, the striction curve is no other than the curve of centres that is used in [23]. In order to eliminate this special case and decrease computation effort, we investigate the use of a Cartesian metric between the closest points from the origin on the expected ISA based on the kinematics model and on the sensed ISA as obtained from an extrinsic sensor.

Although it could be possible to detect a motion discrepancy between the theoretical and actual kinematics by separately monitoring position deviation, orientation deviation, and twist

deviation, it would not be possible to find a single metric with homogeneous units.

Assume that an extrinsic sensor provides the position $\bar{\mathbf{p}}_{g_k}^W$ and orientation $\bar{\mathbf{R}}_{g_k}^W$ of the ED of each segment with respect to a world reference frame $\{W\}$. Without loss of generality, we assume that $\{W\}$ is aligned with $\{B_1\}$. The relative position and orientation of the k th ED with respect to the previous one is given by

$$\bar{\mathbf{p}}_{g_k}^{b_k} = \bar{\mathbf{R}}_{g_k}^{g_{k-1}} (\bar{\mathbf{p}}_{g_k}^W - \bar{\mathbf{p}}_{g_{k-1}}^W) \quad (23)$$

$$\bar{\mathbf{R}}_{g_k}^{g_{k-1}} = \bar{\mathbf{R}}_{g_k}^{b_k} = \bar{\mathbf{R}}_{g_k}^{g_{k-1}} \bar{\mathbf{R}}_{g_k}^W. \quad (24)$$

where all entities marked with a bar (i.e., \bar{p}) are based on sensor measurements. The aforementioned equations provide the decoupled motion of each segment. Using the constrained kinematic model in (4) and (5) with $\sigma_k = 0$ (i.e., no contact), the theoretical relative position, i.e., $\mathbf{p}_{g_k}^{b_k}(\sigma_k = 0)$, and orientation, i.e., $\mathbf{R}_{g_k}^{b_k}(\sigma_k = 0)$, are obtained. The theoretical linear and angular velocities $\mathbf{v}_{g_k/b_k}^{b_k}$ and $\omega_{g_k/b_k}^{b_k}$ are obtained using (6) and (11), respectively. On the other hand, the sensed linear and angular velocities $\bar{\mathbf{v}}_{g_k/b_k}^{b_k}$ and $\bar{\omega}_{g_k/b_k}^{b_k}$ are obtained by numerical differentiation of (23) and (24), respectively, along with the definition of angular velocity. These theoretical and sensed relative poses and velocities are used to define the following SMD:

$$\mu_k = \|\mathbf{r}_k(\sigma_k = 0) - \bar{\mathbf{r}}_k\| \quad (25)$$

where $\bar{\mathbf{r}}_k$ is calculated using (17).

The use of relative motion data for μ_k decouples the SMD's and provides the basis for collision detection and estimation of contact location along any segment of the continuum robot independently.

V. COLLISION DETECTION

Ideally, for a perfect robot, a perfect controller, and a perfect sensor, one would obtain $\mu_k = 0$. However, because of kinematics model approximations, an uncalibrated robot, extension of the actuation lines, and sensor noise, μ_k will be bounded by a certain distance threshold ϵ_k during unconstrained motion. A collision is, therefore, independently detected for any segment when $\mu_k > \epsilon_k$ for $k = 1, 2, \dots, n$.

In the case of electromagnetic tracking devices, threshold ϵ_k is time, position, and velocity dependent because the accuracy varies depending on the workspace and the proximity to ferromagnetic and conductive metals. Although it is possible to improve the accuracy of these devices by recalibrating the device [40], [41], we can assume that nonstatic ferromagnetic objects are present in the proximity of the robot. Furthermore, if a low-order difference method is used for the differentiation of (23) and (24) with respect to time, low velocities amplify the noise components [42] and increase the variance of the SMD. For this reason, the algorithm needs to filter out false positive because of the noise ratio, when $\|\omega_{g_k/b_k}^{b_k}\| < \zeta_k$, where ζ_k is a threshold in radians per second.

This phenomenon is reproduced in simulation and shown in Fig. 4 and multimedia extension II. In Fig. 4(a), we show an unconstrained CS following a quintic polynomial trajectory in

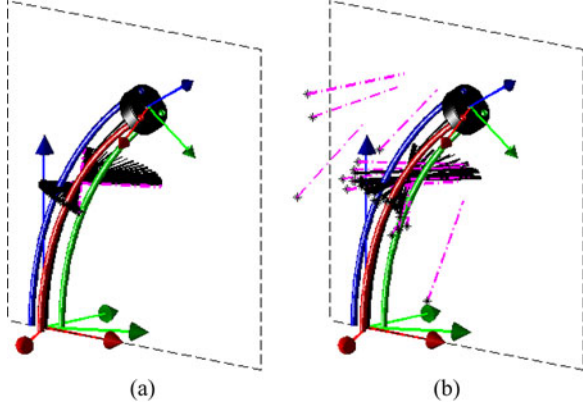


Fig. 4. Comparison of the ISAs for (a) perfect sensor and (b) noisy sensor. The dashed ISA's indicates that the magnitude of the angular velocity is smaller than 0.1 rad/s.

configuration space with its compact axode of motion (i.e., the group of infinitesimally separated ISAs). The dashed ISA's are associated with $\|\omega_{g_k/b_k}^{b_k}\| < \zeta_k$. Since the motion is generated with a quintic polynomial, the dashed ISAs are associated with the beginning and the end of the motion. In Fig. 4(b), we show the CS following the same trajectory but the position and twist of its ED are perturbed with white Gaussian noise. When the magnitude of the noise is comparable with the magnitude of the linear and angular velocities, the screw of motion that is obtained with (18) and (20) loses any physical significance.

If a sensor with the resolution ε_s [rad] collects data with frequency f_s [Hz], then the value of ζ_k must meet the following constraint for trustworthy velocity measurements:

$$\zeta_k > \alpha \varepsilon_s f_s \quad (26)$$

where $\alpha > 1$ (ideally 2 or 3). The threshold value ζ_k is proportional to sensor resolution ε_s and sample frequency f_s and defines the lowest angular velocity of each end disk under which no contact can be reliably detected. There are two ways to reduce the critical angular velocity magnitude ζ_k : increase sensor resolution, or decrease sampling frequency. Although the latter solution decreases threshold ζ_k , it also degrades the responsiveness of the collision-detection algorithm by the introduction of lag into the system. However, since the minimal and maximal allowable twist is generally known once a task is defined, threshold ζ_k can be tuned accordingly.

Thus, we define the following binary function:

$$\mathcal{F}(t) = \begin{cases} 1, & \mu_k > \epsilon_k \\ 0, & \mu_k \leq \epsilon_k. \end{cases} \quad (27)$$

Once $\mu_k > \epsilon_k$ and $\|\omega_{g_k/b_k}^{b_k}\| > \zeta_k$, collision is detected when

$$\sum_{t=t_c}^{t_c+Q\Delta_t} \mathcal{F}(t) = Q \quad (28)$$

where t_c is the first instant in which $\mu_k > \epsilon_k$, Δ_t is time-step constant of the contact-detection algorithm, and Q is the width of the collision-detection window that allows to filter out false positives.

Algorithm 1 Collision detection

Input: L_k {length of k^{th} segment}
Input: $\psi(t)$ {commanded configuration space}
Input: $\dot{\psi}(t)$ {commanded configuration space velocity}
Input: $\bar{\mathbf{r}}_k(t)$ {point from the origin on sensed ISA}
Input: Δ_t {time step}
Input: c_{t-1} {counter variable}
Input: d_{t-1} {collision detection flag at $t - \Delta_t$ }
 $\sigma_k = 0$
if $\|\omega_{g_k/b_k}^{b_k}\| > \zeta_k$ **then**
 $\mathbf{p}_{g_k}^{b_k} \leftarrow$ equation (4) {position of gripper}
 $\mathbf{J}_{v\psi} \leftarrow$ equation (7) {translational Jacobian}
 $\mathbf{J}_{\omega\psi} \leftarrow$ equation (12) {rotational Jacobian}
 $\mathbf{v}_{g_k/b_k}^{b_k} \leftarrow \mathbf{J}_{v\psi} \dot{\psi}_d(t)$ {linear velocity}
 $\omega_{g_k/b_k}^{b_k} \leftarrow \mathbf{J}_{\omega\psi} \dot{\psi}_d(t)$ {angular velocity}
 $\mathbf{r}_k \leftarrow$ equation (20) {point on expected ISA}
 $\mu_k(t) = \|\mathbf{r}_k - \bar{\mathbf{r}}_k(t)\|$ {SMD}
if $\mu_k > \epsilon_k$ **then**
 $c_t = c_{t-1} + 1$
if $d_{t-1} == 1$ **then**
if $c_t \geq Q$ **then**
return 1 {Collision detected}
end if
else
 $d_t = 1$ {start detection window}
end if
else
 $c_t = 0, d_t = 0$
return 0 {No collision}
end if
else
 $c_t = 0, d_t = 0$
return 0 {No Collision}
end if

The collision-detection strategy is described in Algorithm 1. Its inputs are: the nominal length of the segment, i.e., L_k ; the closest point from the origin on the sensed ISA, i.e., $\bar{\mathbf{r}}_k(t)$; the commanded configuration space orientation, i.e., $\psi(t)$; its time derivative, i.e., $\dot{\psi}(t)$; a counter variable c_{t-1} ; a binary variable d_{t-1} ; and the time step Δ_t . The algorithm initializes the contact arc length, i.e., $\sigma_k = 0$, so that the unconstrained model of the CS is used. Thus, it checks if the magnitude of the angular velocity is high enough to have meaningful sensor data. If this is the case, the motion residual is obtained using (4), (7), (12), (6), (11), and (20). Next, it checks for $\mu_k > \epsilon_k$. In the case of detection, the algorithm checks if the collision-detection window was previously started. If so, the counter variable c_{t-1} is incremented and used for future iterations. When the condition in (28) is met, collision is detected.

VI. ESTIMATION OF CONTACT LOCATION

For an n -segment continuum robot, the collision-detection algorithm of Section V already identifies, which segments are constrained by the environment. We, therefore, propose a second

Algorithm 2 Estimation of Contact Location

Input: L_k {length of k^{th} segment}
Input: N {number of disks}
Input: Δ_t {time step}
Input: t_c {instant of contact}
Input: t_f {end of detection window}
Input: $\psi(t_c : t_f)$ {trajectory for $t = t_c, \dots, t_f$ }
Input: $\dot{\psi}(t)$ {commanded configuration space velocity}
Input: $\bar{\mathbf{r}}_k(t_c : t_f)$ {point on sensed ISA for $t = t_c, \dots, t_f$ }

for $\sigma_k = 0 : L_k/N : L_k$ **do**
 $\mathbf{p}_{C_k}^{b_k} \leftarrow$ equation (1) {compute position of C_k }
 $\mathbf{R}_{C_k}^{b_k} \leftarrow$ equation (2) {compute orientation of C_k }
 $\theta_{\sigma_k} \leftarrow$ equation (3) {compute angle at contact location}
for $t = t_c : \Delta_t : t_f$ **do**
 $\mathbf{p}_{g_k}^{b_k} \leftarrow$ equation (4) {position of gripper}
 $\mathbf{J}_{v\psi} \leftarrow$ equation (7) {translational Jacobian}
 $\mathbf{J}_{\omega\psi} \leftarrow$ equation (12) {rotational Jacobian}
 $\mathbf{v}_{g_k/b_k}^{b_k} \leftarrow \mathbf{J}_{v\psi} \dot{\psi}_d(t_c)$ {linear velocity}
 $\boldsymbol{\omega}_{g_k/b_k}^{b_k} \leftarrow \mathbf{J}_{\omega\psi} \dot{\psi}_d(t)$ {angular velocity}
 $\mathbf{r}_k \leftarrow$ equation (20) {closest point on expected ISA}
 $\mu_k(t) = \|\mathbf{r}_k - \bar{\mathbf{r}}_k(t)\|$ {SMD}
end for
 $\tilde{\mu}_k \leftarrow \frac{1}{\Delta_t(t_f - t_c)} \sum \|\mu_k\|_{\sigma_k, t}$ {median of the SMD's}
end for
return σ_k with smallest $\tilde{\mu}_k$

algorithm that narrows down the estimation of contact location at the segment level. The main assumption is that, immediately after collision, the constrained segment behaves according to assumption A4. This assumption was experimentally verified in [23] for a single segment with a fixed base during planar motion. In the case of multiple segments, this assumption is still valid if the stiffness of two subsequent segments is comparable. The stiffness of constrained segment $k + 1$ needs to be high enough to prevent the motion of segments $k = 1, \dots, k$. This assumption is experimentally evaluated in Section VIII-D, where the algorithm is used with a three-segment continuum robot in which the distal segment is very compliant. Results show that the estimation of the location at the third segment is less effective because assumptions A3 and A4 are violated.

The estimation method is described in Algorithm 2. Input N is the parameter that defines the level of discretization for the estimation. In the case of the continuum robot that is shown in Fig. 5, the contact is most likely to occur at any of the SD that are placed L_k/N apart from each other. Input Δ_t is the time step that is associated with the extrinsic sensor. Inputs t_c and t_f are the first and last instants of the detection window that is initiated by Algorithm 1. Inputs $\psi(t_c : t_f)$ and $\bar{\mathbf{r}}_k(t_c : t_f)$ are, respectively, the desired configuration space trajectory and the time history of closest point on the sensed ISA. Once the algorithm is initialized, the algorithm collects the SMD's associated with each guessed σ_k and finds the arithmetic mean of the SMD for instants of time included into the detection window. The method finally returns the contact arc length σ_k that is associated with the smallest SMD.

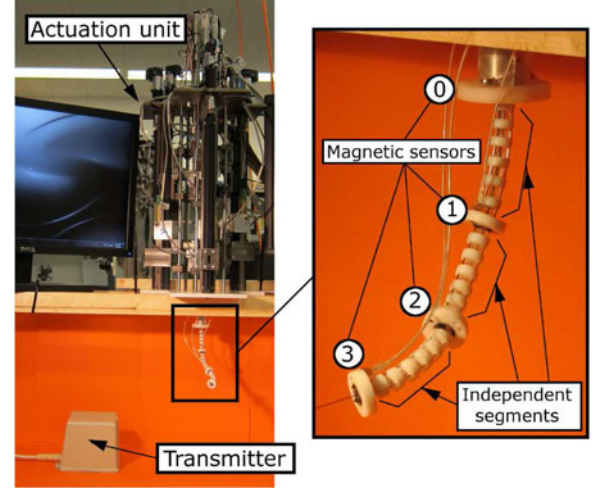


Fig. 5. The experimental setup consist of a nine-axis actuation unit, a three-segment continuum robot, a magnetic-field transmitter, and four magnetic sensors that are attached to the robot's base ①, first segment's end disk ①, second segment's end disk ②, and robot's end effector ③.

TABLE II
ROBOT'S SPECIFICATIONS AND COLLISION THRESHOLDS

	segment 1	segment 2	segment 3
L [mm]	50	50	45
disk height [mm]	3.5	3.5	3.5
spacing [mm]	3.6	3.6	3.4
# of disks	7	7	6
ϵ_k [mm]	10	8	8
ζ_k [rad/s]	0.1	0.1	0.1

The accuracy of the estimation of contact location algorithm not only depends on the modeling arguments that are described in Section III but is affected by the discretization parameter N as well. The smaller this value is, the finer the minimization problem is. For the robot shown in Fig. 5, N is equal to the number of SD. This means that the algorithm will only return the disk at which the contact is most likely to occur. Contacts in between two adjacent SD's will be associated with one of the two disks. This phenomenon will be shown in Section VIII-D.

VII. EXPERIMENTAL SETUP

The experimental setup that is shown in Fig. 5 consists of a 6-DOF three-segment multibackbone continuum robot (see the specifications reported in Table II), and an Ascension 3-D Guidance trakSTAR electromagnetic tracker. This device has an RMS accuracy of 1.4 mm in position and 0.5° in orientation [43]. The robot is equipped with four 6-DOF Model: 130 sensors placed at the robot's base (0), first segment ED (1), second segment ED (2), and end-effector (3), respectively.

The continuum robot is controlled with the mixed configuration- and joint-space feedback architecture shown in Fig. 6. The configuration space feedback is provided by the same sensor that is used in the collision detection and estimation of contact location algorithms. This additional feedback reduces the configuration space tracking error but does not affect the task-space tracking error. This discrepancy is the base of the algorithms that are presented in Sections V and VI. In the

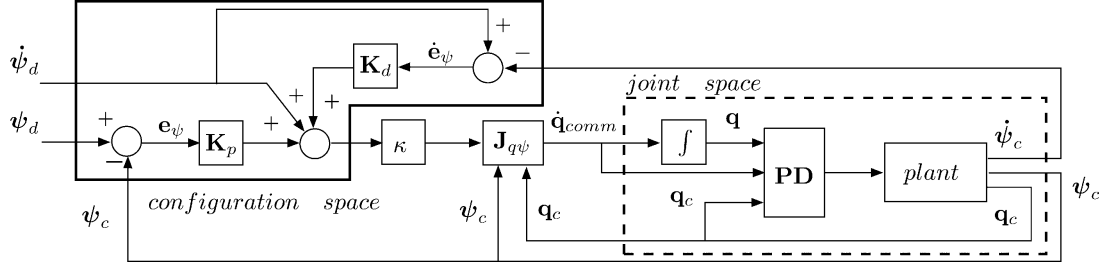


Fig. 6. Block diagram of the proposed tiered mixed feedback controller for multisegment multibackbone continuum robots.

remainder of this section, we briefly introduce the configuration space controller. The proof of stability and performances of the tiered controller are reported in [30].

We introduce the *configuration space error* e_ψ as the deviation of the current configuration space vector ψ_c from the desired configuration space vector ψ_d :

$$e_\psi = \psi_d - \psi_c. \quad (29)$$

The time derivative of (29) when accounting for (16) and the compensation factor $\kappa > 1$ that is presented in [27] yields

$$\dot{e}_\psi = \dot{\psi}_d - \eta \kappa \mathbf{J}_{q\psi}^\dagger \dot{q}_{comm} \quad (30)$$

where superscript “ \dagger ” denotes the pseudoinverse, \dot{q}_{comm} is the commanded augmented vector of joint speeds, and η is a positive scalar that corresponds to sensor and plant uncertainties. The control input to the low-level joint-space controller is given by

$$\dot{q}_{comm} = \kappa \mathbf{J}_{q\psi} \left(\dot{\psi}_d + \mathbf{K}_p e_\psi + \mathbf{K}_d \dot{e}_\psi \right). \quad (31)$$

VIII. EXPERIMENTAL VALIDATION

In this section, we present experiments of single-contact collision detection, multicontact collision detection, collision-detection repeatability, and estimation of contact location. In all experiments, the robot of Fig. 5 was commanded from the starting configuration, i.e., $\psi_s = [72^\circ \ 0^\circ \ 72^\circ \ 0^\circ \ 72^\circ \ 45^\circ]^T$, to the final configuration, i.e., $\psi_f = [45^\circ \ 45^\circ \ 45^\circ \ -45^\circ \ 45^\circ \ 45^\circ]$, using a quintic polynomial trajectory with zero initial and final velocity, zero initial and final acceleration, and accomplishment time of 5 s in configuration space.

A. Single-Contact Collision Detection

The first set of experiments demonstrate the ability of the collision-detection algorithm to detect a single collision acting along the continuum robot. Results are presented in Figs. 7–9. The vertical lines that are labeled *detection enabled* and *detection disabled* designate beginning and end of the portion of the motion with the angular velocity magnitudes bigger than $\zeta_k = 0.1$ rad/s as described in Algorithm 1.

First, the first segment of the continuum robot is constrained during the motion. The time histories of SMDs, i.e., μ_1 , μ_2 , and μ_3 , as defined in (25) are presented in Fig. 7. The SMD of the first segment [see Fig. 7(a)] rises above the threshold at approximately $t = 15$ s. After a detection window of a half second, collision is successfully triggered. The SMDs that are

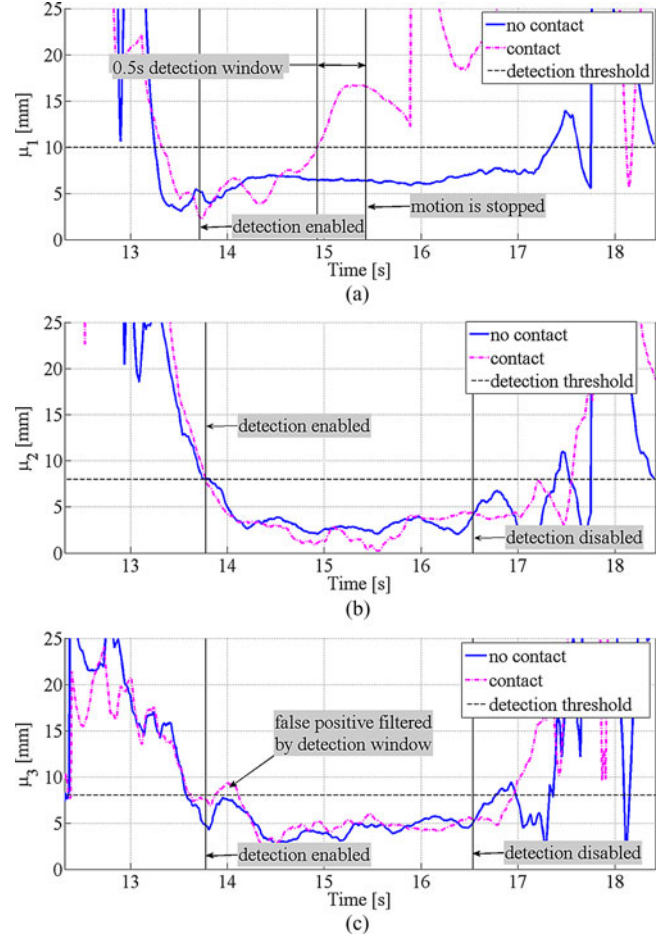


Fig. 7. Constraint acting at the first segment. (a) Time history of μ_1 . (b) Time history of μ_2 . (c) Time history of μ_3 .

associated with the second and third segments [see Fig. 7(b) and (c), respectively] are not affected by the constraint.

Second, the second segment of the continuum robot is constrained during the motion. The time histories of SMDs, i.e., μ_1 , μ_2 , and μ_3 , are presented in Fig. 8. A collision is detected at the second segment [see Fig. 8(b)] at approximately $t = 14.9$ s after a collision-detection window of the half second. The SMD μ_1 that is associated with the first segment is also affected by the contact and rises above the threshold at approximately $t = 14.8$ s. This delay is because of the compliance of the segments and allows to distinguish between single and multiple collisions, as shown in Section VIII-B. In addition, in

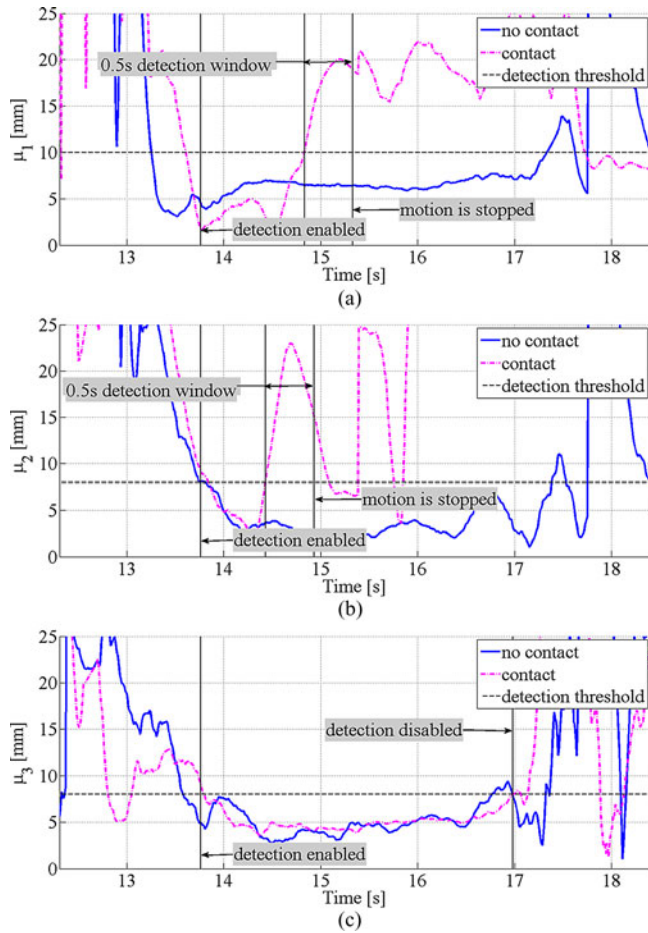


Fig. 8. Constraint acting at the second segment. (a) Time history of μ_1 . (b) Time history of μ_2 . (c) Time history of μ_3 .

this case, the SMD μ_3 that is associated with the third segment remains unaffected.

Third, the third segment of the continuum robot is constrained during the motion. The time histories of SMDs, i.e., μ_1 , μ_2 , and μ_3 , are presented in Fig. 9. Collision is detected at the third segment at $t = 14.95$ s [see Fig. 9(c)]. Similar to the previous case, the two proximal segment are also affected by the contact as shown by their respective SMD's [see Fig. 9(a) and (b)].

These experiments are shown in the multimedia extension III—Part I. The video also demonstrate the ability of the collision-detection algorithm to successfully detect collisions with a soft constraint and other continuum arms. This capability is of primary importance when the algorithm is implemented on surgical continuum robots and surgical robotic systems with continuum end effectors [44]. The collision-detection algorithm would be able to prevent inadvertent trauma to delicate surrounding tissues by triggering a reaction strategy as in [10].

B. Multicontact Collision Detection

The second set of experiments demonstrate the ability of the collision-detection algorithm to detect multiple collisions. We assume that the constraints act on different segments of the robot and that in the case of a two-contact collision, the proximal seg-

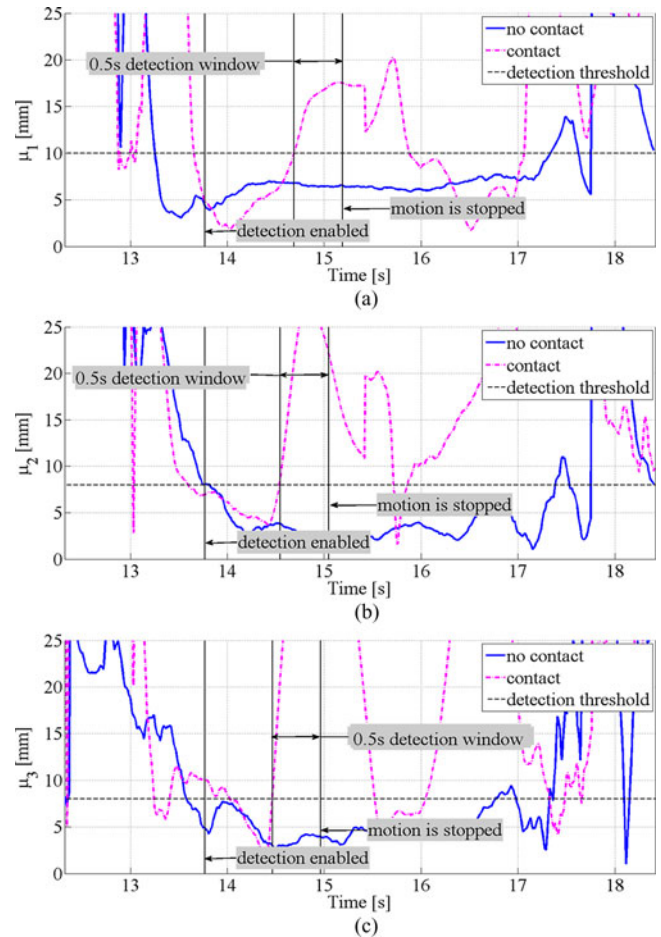


Fig. 9. Constraint acting at the third segment. (a) Time history of μ_1 . (b) Time history of μ_2 . (c) Time history of μ_3 .

ment collides first. This is possible by using one of the reaction strategies that are proposed in [10]: once the collision is detected, the motion of the constrained segments is stopped, while the unconstrained segments continue the preplanned trajectory. In Fig. 10, we show the time histories of the SMDs, i.e., μ_1 , μ_2 , and μ_3 . A collision with the first segment is detected at approximately $t = 14.2$ s [see Fig. 10(a)]. The detection window is initiated immediately after the collision detection is enabled. A collision at the second segment is detected at approximately $t = 15$ s [see Fig. 10(b)]. The main difference between Figs. 8 and 10 is the order in which collisions are detected. In Fig. 8, collision is first detected at the second segment and, then, at the first segment. On the other hand, in Fig. 10, a collision is first detected at the first segment and then at the second segment. The order in which the collisions are detected allows for discerning between a single contact acting at the second segment and multiple contacts acting at the first and second segments. Similarly to the previous case studies, the SMD that is associated with the third segment is not affected, and no collision is detected [see Fig. 10(c)].

Multimedia extension III—Part II shows the multisegment continuum robot of Fig. 5 detecting multiple collisions acting at

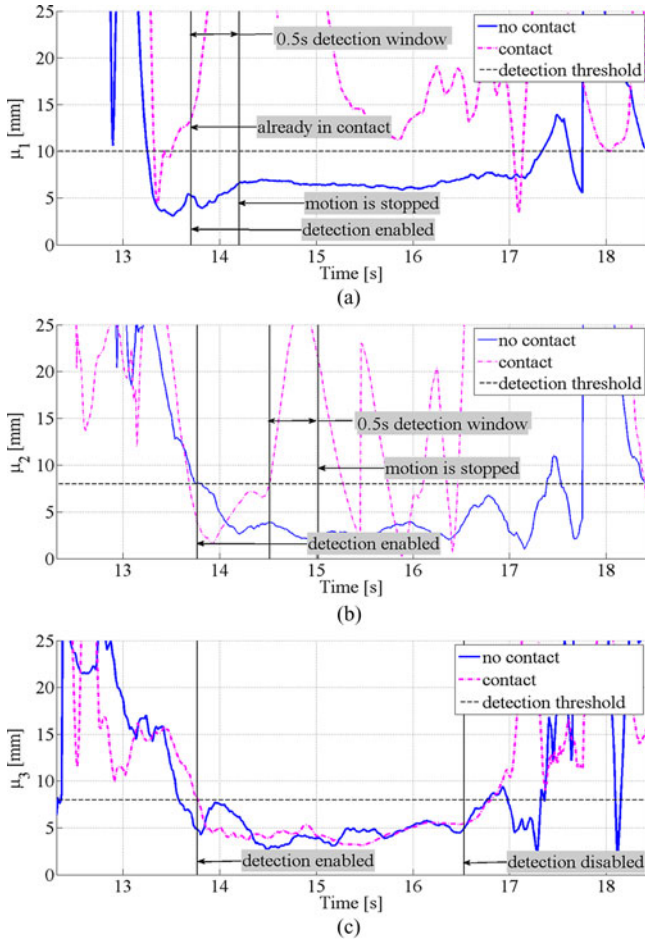


Fig. 10. Detection of multiple collisions. (a) Time history of μ_1 . (b) Time history of μ_2 . (c) Time history of μ_3 .

multiple segments and on the entire flexible structure, as shown in Fig. 1(c).

C. Repeatability of Collision Detection

Additional experiments were conducted to quantify the repeatability of the collision-detection algorithm. The second segment of the continuum robot impacted a static, rigid object ten times. The constraining object is a carbon fiber tube covered with silicon material to increase friction at the contact point and reduce slippage. The time history of the SMD μ_2 for all ten trials is shown in Fig. 11. The instant of collision varies by only 0.07 s demonstrating a very high repeatability.

D. Estimation of Contact Location

The last set of experiments evaluates the performance of the estimation algorithm. Each experiment is repeated five times, and the obstacle is adjusted to constrain one of the SD's of the continuum robot. However, because of the small size of the robot, contact can occur at any location along the disk's height (see Table II).

Results are reported in Tables III–V. Column d_i indicates the disk that is impacted, and column T indicates the experiment

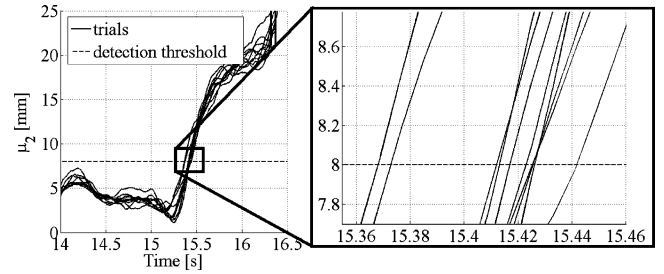


Fig. 11. Repeatability analysis of contact detection. Time history of μ_2

TABLE III
CONTACT ESTIMATION ALONG THE FIRST SEGMENT

d_i	T	d_0	d_1	d_2	d_3	d_4	d_5	d_6	d_7
3	1	9.2	6.0	3.4	3.6	6.3	9.6	13.0	16.5
	2	7.7	4.7	3.0	4.7	7.8	11.1	14.6	18.0
	3	9.8	6.4	3.5	2.9	5.4	8.7	12.2	15.7
	4	9.8	6.6	4.1	3.9	6.2	9.4	12.7	16.1
	5	10.4	7.1	4.2	3.2	5.3	8.4	11.8	15.2
4	1	11.7	8.4	5.6	4.1	5.2	7.9	11.1	14.5
	2	11.9	8.7	6.0	4.5	5.4	8.0	11.0	14.4
	3	11.7	8.6	6.0	4.6	5.7	8.3	11.4	14.7
	4	11.7	8.5	5.7	4.7	5.2	7.9	11.1	14.4
	5	11.3	8.1	5.2	3.7	5.1	7.9	11.2	14.6
5	1	14.6	11.3	8.2	5.4	3.8	5.0	7.7	10.8
	2	15.0	11.6	8.3	5.3	3.1	4.0	6.9	10.1
	3	15.6	12.4	9.2	6.3	4.3	4.7	7.0	10.0
	4	16.2	12.9	9.7	7.1	5.3	5.4	7.4	10.2
	5	15.6	12.5	9.7	7.5	6.4	7.1	9.1	11.8

Units of millimeters.

trial number. The remaining eight columns d_0, \dots, d_7 report the arithmetic average of the SMD that is associated with each guessed constrained disk locations as described in Algorithm 2. In particular, d_0 represents the BD (i.e., no contact) and d_7 represents the ED (i.e., segment completely constrained). In each row, the entry that is associated with the smallest SMD is highlighted in gray.

Experimental results of the estimation of contact location on the proximal segment of the continuum robot are presented in Table III. Very small SMD's for two consecutive disks (3.64 mm apart from each other) are reported. This discrepancy in the estimation of the location of contact corresponds to a worst-case-scenario error of at most the height of two SD's and the space between two adjacent disks (see Table II). The sources of uncertainty and the possible slippage of the robot with respect to the rod indicate that the error in the estimation of the contact location within one disk error is indeed expected.

Experimental results of the estimation of contact location on the second segment of the continuum robot are presented in Table IV. The success rate of the algorithm is appreciably higher than the previous case study. The improvement is because of a better noise/signal ratio and a smaller collision threshold, as shown in Fig. 8(a) and (b). The third disk is successfully identified four out of five times, and the fourth disk is successfully identified five out of five times. In the case of the second and fifth disks, the algorithm reports a very small deviation between consecutive disks 1, 2 and 5, 6.

Experimental results of the estimation of contact location on the second segment of the continuum robot are presented in

TABLE IV
CONTACT ESTIMATION ALONG THE SECOND SEGMENT

d_i	T	d_0	d_1	d_2	d_3	d_4	d_5	d_6	d_7
2	1	7.0	5.8	6.3	8.4	11.0	14.1	17.2	20.4
	2	5.9	4.7	5.7	8.1	11.1	14.3	17.6	20.9
	3	6.3	4.5	5.0	7.4	10.4	13.7	17.0	20.4
	4	7.8	6.5	6.7	8.4	10.9	13.8	16.9	20.0
	5	6.1	3.9	4.1	6.7	9.8	13.1	16.5	19.9
3	1	11.8	10.4	9.9	10.5	12.0	14.0	16.5	19.3
	2	13.1	11.2	10.0	9.7	10.6	12.3	14.6	17.2
	3	13.2	11.3	10.1	9.9	10.7	12.3	14.7	17.3
	4	13.0	11.0	9.6	9.2	10.0	11.7	14.1	16.8
	5	13.1	11.1	9.8	9.5	10.4	12.1	14.4	17.1
4	1	18.1	15.8	13.8	12.4	11.7	11.9	13.0	14.8
	2	17.9	15.4	13.3	11.8	10.9	11.1	12.2	14.0
	3	17.6	15.2	13.2	11.7	11.1	11.4	12.6	14.4
	4	18.7	16.3	14.2	12.6	11.6	11.6	12.4	14.0
	5	17.8	15.2	13.2	11.6	10.9	11.1	12.2	14.1
5	1	20.3	17.1	13.9	10.7	7.8	5.6	5.1	6.7
	2	22.2	19.2	16.4	13.7	11.4	9.7	9.0	9.5
	3	21.6	18.7	16.0	13.5	11.4	10.0	9.6	10.4
	4	22.0	19.0	16.3	13.7	11.5	10.0	9.5	10.1
	5	21.0	18.1	15.3	12.7	10.5	9.1	8.9	9.9

Units of millimeters.

TABLE V
CONTACT ESTIMATION ALONG THE THIRD SEGMENT

d_i	T	d_0	d_1	d_2	d_3	d_4	d_5	d_6	d_7
2	1	7.6	5.1	3.8	4.8	7.3	10.1	13.2	16.2
	2	8.7	7.3	7.0	8.1	10.0	12.5	15.2	18.0
	3	5.1	3.4	4.2	6.7	9.7	12.7	15.8	18.9
	4	5.3	4.4	5.5	7.9	10.7	13.6	16.6	19.7
	5	7.2	6.7	7.4	9.3	11.7	14.4	17.2	20.1
3	1	12.2	9.4	6.9	5.1	4.9	6.6	9.0	11.8
	2	15.7	13.2	10.9	9.0	8.0	8.1	9.2	11.1
	3	14.8	12.6	10.7	9.4	9.0	9.6	11.0	13.0
	4	15.3	12.4	9.6	7.0	5.2	5.0	6.5	8.9
	5	15.1	12.6	9.3	6.4	5.8	6.2	7.1	11.2
4	1	12.0	10.2	9.1	9.0	9.8	11.4	13.6	16.0
	2	14.5	11.8	9.3	7.2	6.0	6.3	7.9	10.3
	3	12.6	10.7	9.5	9.0	9.5	10.9	12.9	15.2
	4	13.6	10.9	8.6	6.9	6.3	7.1	9.0	11.4
	5	11.6	9.6	7.6	6.8	7.3	8.9	11.1	13.6

Units of millimeters.

Table V. The performance of the estimation algorithm appear to be more problematic because Assumption A4 is violated, as shown in multimedia extension III—Part III. The lower stiffness of the third CS results in dramatic deformation of the segment, invalidating the constrained kinematic model that is presented in Section III-B.

IX. CONCLUSION

In this paper, the first unified framework for collision detection and localization of contacts along multisegment continuum robots has been proposed. The need of these algorithms stems from the field of medical robotics. Pioneering surgical procedures demand deeper anatomical reach along increasingly tortuous paths. Future medical robots that are built to meet the challenges of NOTES will need to autonomously prevent inadvertent trauma to surrounding anatomy, while accomplishing telerobotic surgical tasks beyond the capabilities of conventional robotic platforms for minimally invasive surgery (MIS). Previous works on rigid-link robots do not apply directly to continuum manipulators and do not provide a unified method

for both collision detection and estimation of contact location without *a priori* knowledge of the environmental constraints and additional sensory devices, such as robotic skins.

The collision-detection algorithm that is presented in this paper offers the immediate application for safeguarding against inadvertent anatomical trauma in robotic systems that is equipped with multiple continuum arms. Results show the effectiveness of the algorithm even in detecting contact with soft objects, like human fingers and other continuum arms. There are consistent margins for decreasing the detection thresholds after proper calibration of the magnetic tracker device and kinematics parameters of the robot. Despite this, the adoption of the motion deviation that has been described in this paper already allows for robust collision detection.

The estimation of contact location is shown to be effective in the case in which the stiffness of all the individually actuated segments is comparable. When this fundamental assumption is violated (as in the third segment), the proposed constrained kinematic model fails to describe the constrained motion. Future work will focus on the improvement of the performance of the estimation of contact location using probabilistic inference and Kalman filtering.

REFERENCES

- [1] O. Khatib, "A unified approach for motion and force control of robot manipulators: The operational space formulation," *IEEE J. Robot. Autom.*, vol. RA-3, no. 1, pp. 43–53, Feb. 1987.
- [2] A. De Luca and C. Manes, "Modeling of robots in contact with a dynamic environment," *IEEE Trans. Robot. Autom.*, vol. 10, no. 4, pp. 542–548, Aug. 1994.
- [3] B. Siciliano and L. Villani, *Robot Force Control*. Boston, MA: Kluwer, 1999.
- [4] J. Park and O. Khatib, "Robot multiple contact control," *Robotica*, vol. 26, no. 5, pp. 667–677, 2008.
- [5] L. Sentis, J. Park, and O. Khatib, "Compliant control of multicontact and center-of-mass behaviors in humanoid robots," *IEEE Trans. Robot.*, vol. 26, no. 3, pp. 483–501, Jun. 2010.
- [6] M. H. Raibert and J. J. Craig, "Hybrid position/force control of manipulators," *ASME J. Dyn. Syst. Meas. Control*, vol. 102, pp. 126–133, 1981.
- [7] M. T. Mason and J. K. Salisbury, *Robot Hands and the Mechanics of Manipulation*. Cambridge, MA: MIT Press, 1985.
- [8] H. Lipkin and J. Duffy, "Hybrid twist and wrench control for a robotic manipulator," *Trans. ASME*, vol. 110, pp. 138–144, 1988.
- [9] R. Featherstone, "Modeling and control of contact between constrained rigid bodies," *IEEE Trans. Robot. Autom.*, vol. 20, no. 1, pp. 82–92, Feb. 2004.
- [10] A. De Luca, S. Haddadin, and G. Hirzinger, "Collision detection and safe reaction with the DLR-III lightweight manipulator srm," in *Proc. IEEE/RSJ Int. Conf. Intell. Robots Syst.*, Beijing, China, 2006, pp. 1623–1630.
- [11] S. Haddadin, A. De Luca, and G. Hirzinger, "Collision detection and reaction: A contribution to safe physical human–robot interaction," in *Proc. IEEE/RSJ Int. Conf. Intell. Robots Syst.*, Nice, France, 2008, pp. 3356–3363.
- [12] B. S. Eberman and J. K. Salisbury, *Determination of Manipulator Contact Information from Joint Torque Measurements*, vol. 139. New York: Springer-Verlag, 1990, pp. 463–473.
- [13] T. J. Debus, P. E. Dupony, and R. D. Howe, "Contact state estimation using multiple model estimation and hidden Markov models," *Int. J. Robotics Res.*, vol. 24 no. 4-5, pp. 399–413, 2003.
- [14] A. Petrovskaya, J. Park, and O. Khatib, "Probabilistic estimation of whole body contacts for multicontact robot control," in *Proc. IEEE Int. Conf. Robot. Autom.*, Rome, Italy, 2007, pp. 568–573.
- [15] V. J. Lumelsky and E. Cheung, "Real-time collision avoidance in teleoperated whole-sensitive robot arm manipulators," *IEEE Trans. Syst., Man, Cybern.*, vol. 23, no. 1, pp. 194–203, Jan./Feb. 1993.

- [16] R. J. Webster, III and B. A. Jones, "Design and kinematic modeling of constant curvature continuum robots: A review," *Int. J. Robot. Res.*, vol. 29, no. 13, pp. 1661–1683, 2010.
- [17] N. Simaan, "Snake-like units using flexible backbones and actuation redundancy for enhanced miniaturization," in *Proc. IEEE Int. Conf. Robot. Autom.*, Barcelona, Spain, 2005, pp. 3023–3028.
- [18] P. Dupont, J. Lock, B. Itkowitz, and E. Butler, "Design and control of concentric-tube robots," *IEEE Trans. Robot.*, vol. 26, no. 2, pp. 209–225, Apr. 2010.
- [19] R. J. Webster, III, J. M. Romano, and N. J. Cowan, "Mechanics of precurved-tube continuum robots," *IEEE Trans. Robot.*, vol. 25, no. 1, pp. 67–78, Feb. 2009.
- [20] D. B. Camarillo, C. F. Milne, C. R. Carlson, M. R. Zinn, and J. K. Salisbury, "Mechanics modeling of tendon-driven continuum manipulators," *IEEE Trans. Robot.*, vol. 24, no. 6, pp. 1262–1273, Dec. 2008.
- [21] K. Ikuta, K. Yamamoto, and K. Sasaki, "Development of remote microsurgery robot and new surgical procedure for deep and narrow space," in *Proc. IEEE Int. Conf. Robot. Autom.*, Taipei, Taiwan, 2003, pp. 1103–1108.
- [22] K. Xu and N. Simaan, "Intrinsic wrench estimation and its performance index for multisegment continuum robots," *IEEE Trans. Robot.*, vol. 26, no. 3, pp. 555–561, Jun. 2010.
- [23] A. Bajo and N. Simaan, "Finding lost wrenches: Using continuum robots for contact detection and estimation of contact location," in *Proc. IEEE Int. Conf. Robot. Autom.*, Anchorage, AK, 2010, pp. 3666–3673.
- [24] E. R. Goldman, A. Bajo, and N. Simaan, "Compliant motion control for continuum robots with intrinsic actuation sensing," in *Proc. IEEE Int. Conf. Robot. Autom.*, Shanghai, China, 2011, pp. 1126–1132.
- [25] B. A. Jones and I. D. Walker, "Kinematics for multisection continuum robots," *IEEE Trans. Robot.*, vol. 22, no. 1, pp. 43–57, Feb. 2006.
- [26] K. Xu and N. Simaan, "Analytic formulation for kinematics, statics, and shape restoration of multibackbone continuum robots via elliptic integrals," *ASME J. Mech. Robot.*, vol. 2, no. 1, pp. 011006-1–011006-13, 2010.
- [27] K. Xu and N. Simaan, "An investigation of the intrinsic force sensing capabilities of continuum robots," *IEEE Trans. Robot.*, vol. 24, no. 3, pp. 576–587, Jun. 2008.
- [28] D. B. Camarillo, C. R. Carlson, and J. K. Salisbury, "Configuration tracking for continuum manipulators with coupled tendon drive," *IEEE Trans. Robot.*, vol. 25, no. 4, pp. 798–808, Aug. 2009.
- [29] J. M. Croom, D. C. Rucker, J. M. Romano, and R. J. Webster, III, "Visual sensing of continuum robot shape using self-organizing maps," in *Proc. IEEE Int. Conf. Robot. Autom.*, Anchorage, AK, 2010, pp. 4591–4596.
- [30] A. Bajo, R. E. Goldman, and N. Simaan, "Joint and configuration feedback for enhanced performance of multisegment continuum robots," in *Proc. IEEE Int. Conf. Robot. Autom.*, Shanghai, China, 2011, pp. 2905–2912.
- [31] N. Simaan, R. H. Taylor, and P. Flint, "A dexterous system for laryngeal surgery," in *Proc. IEEE Int. Conf. Robot. Autom.*, New Orleans, LA, 2004, pp. 351–357.
- [32] J. Angeles, *Fundamentals of Robotic Mechanical Systems: Theory, Methods, and Algorithms*. New York: Springer-Verlag, 2007.
- [33] J. Angeles, "Automatic computation of the screw parameters of rigid-body motions—Part I: Finitely-separated positions," *ASME J. Dyn. Syst. Meas. Control*, vol. 108, pp. 32–38, 1986.
- [34] J. Angeles, "Automatic computation of the screw parameters of rigid-body motions—Part II: Infinitesimally-separated positions," *ASME J. Dyn. Syst. Meas. Control*, vol. 108, pp. 39–43, 1986.
- [35] O. Bottema and B. Roth, *Theoretical Kinematics*. New York: Dover, 1979.
- [36] E. H. Bokelberg, K. H. Hunt, and P. R. Ridley, "Spatial motion—Part I: Points of inflection and the differential geometry of screws," *Mech. Mach. Theory*, vol. 27, no. 1, pp. 1–15, 1992.
- [37] Y. Zhang and K.-L. Ting, "Point-line distance under Riemannian metrics," *J. Mech. Design*, vol. 130, no. 9, p. 092304, 2008.
- [38] H. Pottmann and J. Wallner, *Computational Line Geometry*. New York: Springer-Verlag, 1999.
- [39] A. Wolf and A. Degani, "Classifying knee pathologies using instantaneous screws of the six degrees-of-freedom knee motion," in *Proc. IEEE Int. Conf. Robot. Autom.*, Orlando, FL, 2006, pp. 2946–2951.
- [40] W. Birkfellner, F. Watzinger, F. Wanschitz, R. Ewers, and H. Bergmann, "Calibration of tracking systems in a surgical environment," *IEEE Trans. Med. Imag.*, vol. 17, no. 5, pp. 737–42, Oct. 1998.
- [41] M. Ikits, J. D. Brederson, C. D. Hansen, and J. M. Hollerbach, "An improved calibration framework for electromagnetic tracking devices," in *Proc. IEEE Virtual Reality*, Yokohama, Japan, 2001, pp. 63–70.
- [42] J. Zhou, X. Shen, E. M. Petriu, and N. D. Georganas, "Linear velocity and acceleration estimation of 3-DOF haptic interface," in *Proc. IEEE Int. Workshop Hapt. Audio Vis. Environ. Appl.*, Ottawa, ON, Canada, 2008, pp. 137–142.
- [43] Ascension Technol. (2011). [Online]. Available: <http://www.ascension-tech.com/realtime/RTtrakSTAR.php>.
- [44] J. Ding, K. Xu, R. E. Goldman, P. K. Allen, D. L. Fowler, and N. Simaan, "Design, simulation and evaluation of kinematic alternatives for insertable robotic effectors platforms in single port access surgery," in *Proc. IEEE Int. Conf. Robot. Autom.*, Anchorage, AK, 2010.



Andrea Bajo (S'10) received the first-level *Laurea* degree in control engineering from the University of Rome "La Sapienza," Rome, Italy, in 2007 and the M.Sc. degree in mechanical engineering from Columbia University, New York, NY, in 2009. He is currently working toward the Ph.D. degree with the Department of Mechanical Engineering, Vanderbilt University, Nashville, TN.

His research interests include kinematics, collision detection, estimation of constraints, dynamics, and control of continuum robots for surgical

applications.



Nabil Simaan (M'04) received the B.Sc., M.Sc., and Ph.D. degrees all in mechanical engineering from the Technion—Israel Institute of Technology, Haifa, Israel, in 1996, 1999, and 2002, respectively.

During 2003, he was a Postdoctoral Research Scientist with National Science Foundation (NSF) Engineering Research Center for Computer-Integrated Surgical Systems and Technology, Johns Hopkins University, Baltimore, MD, where he was involved in research on minimally invasive robotic assistance in confined spaces. In 2005, he joined Columbia Uni-

versity, New York, NY, as an Assistant Professor of mechanical engineering and the Director of the Advanced Robotics and Mechanisms Applications Laboratory. He was promoted to Associate Professor in 2010. He has been with the Department of Mechanical Engineering, Vanderbilt University, Nashville, TN, since the Fall semester of 2010.

Dr. Simaan received the NSF Career award for young investigators to design new algorithms and robots for safe interaction with anatomy in 2009.